

Fractional Chern insulator on a triangular lattice of strongly correlated t_{2g} electrons

Stefanos Kourtis, Jörn W.F. Venderbos, and Maria Daghofer

Institute for Theoretical Solid State Physics, IFW Dresden, 01171 Dresden, Germany

(Dated: October 29, 2018)

We discuss the low-energy limit of three-orbital Kondo-lattice and Hubbard models describing t_{2g} orbitals on a triangular lattice near half-filling. We analyze how very flat single-particle bands with non-trivial topological character, a Chern number $C = \pm 1$, arise both in the limit of infinite on-site interactions as well as in more realistic regimes. Exact diagonalization is then used to investigate an effective one-orbital spinless-fermion model at fractional fillings including nearest-neighbor interaction V ; it reveals signatures of fractional Chern insulator (FCI) states for several filling fractions. In addition to indications based on energies, e.g. flux insertion and fractional statistics of quasiholes, Chern numbers are obtained. It is shown that FCI states are robust against disorder in the underlying magnetic texture that defines the topological character of the band. We also investigate competition between a FCI state and a charge density wave (CDW) and discuss the effects of particle-hole asymmetry and Fermi-surface nesting. FCI states turn out to be rather robust and do not require very flat bands, but can also arise when filling or an absence of Fermi-surface nesting disfavor the competing CDW. Nevertheless, very flat bands allow FCI states to be induced by weaker interactions than those needed for more dispersive bands.

I. INTRODUCTION

Quantum liquids are among the most sought after states of matter. One celebrated class of such quantum liquids, the fractional quantum-Hall (FQH) states,¹⁻³ has been a locus of scientific attention for almost three decades. Initially introduced to explain the fractional quantum-Hall effect (FQHE) observed in semiconductor devices,⁴ they describe interacting electrons constrained in two dimensions and subject to a strong perpendicular magnetic field. Fractionally filling a magnetic Landau level (LL) then yields an incompressible FQH liquid and gives rise to a precisely quantized Hall conductivity. In addition, the quasiparticles of these states obey anyonic statistics,^{5,6} which can be either Abelian or non-Abelian, the latter fulfilling an essential condition for fault-tolerant quantum computation.⁷

An alternative route to quantum Hall liquids is via tightly bound electrons moving in a magnetic texture. The simplest such magnetic texture is a uniform magnetic field perpendicular to the plane of the system. For non-interacting, tightly bound electrons, this gives rise to an integer quantum-Hall (IQH) state and leads to Hofstadter's fractal energy spectrum,⁸ whereas in a fractionally filled tight-binding model of electrons interacting via a screened Coulomb repulsion, the realization of a FQH state is possible.⁹ Haldane noted¹⁰ that an external magnetic field is not the only viable path to IQH states and introduced a honeycomb-lattice model, with complex hoppings that break time-reversal invariance, and defined the first integer Chern insulator (CI), in which the total magnetic field through the unit cell averages to zero. In the meantime, mechanisms leading to complex hoppings with the necessary properties have been identified. One realization may be found in strongly spin-orbit coupled semiconductor materials that are ferromagnetically ordered.^{11,12} Another possibility arises through the coupling of itinerant electrons to localized magnetic mo-

ments,¹³ for example the Kondo-lattice model on the triangular lattice supports a non-trivial magnetic texture, which induces an integer-quantized Hall conductivity of the itinerant electrons.¹⁴

A considerable body of recent research has addressed the question whether the lattice counterpart of the FQHE can be observed when topologically non-trivial bands, called Chern bands, are fractionally filled and electrons are interacting. Several numerical studies using exact diagonalization techniques have convincingly established the existence of Laughlin-series states in an number of different models on various lattices.¹⁵⁻²¹ These systems have since been called fractional Chern insulators (FCI). Very recent work has reported FCI states beyond Laughlin fractions.²²⁻²⁴ In addition to reproducing the known FQHE on a lattice and potentially at higher temperatures, CIs also offer the intriguing possibility of a Chern number higher than one, a departure from the analogy with LLs. Recent studies have explored this direction by constructing models that have higher Chern numbers and studying possible FCI states.²⁵⁻³⁰ From the analytical side, the problem of FCI states has been approached by a careful study of emergent translational symmetries³¹ and many-body trial wave functions.³²⁻³⁴ Others have examined the algebraic properties of the density operators projected onto one Chern band and made a comparison with the Girvin-MacDonald-Platzman algebra that is satisfied by the lowest LL density operators in the continuum FQHE.^{31,35-38}

In numerical studies of FCI states, one typically starts by adding inter-site interactions to topologically nontrivial but non-interacting CI models. As potential realizations of the non-interacting and nearly flat "parent" bands, cold atoms,¹⁶ oxide heterostructures,³⁹ strained graphene,⁴⁰ and strongly correlated multi-orbital models for layered oxides^{22,41} have been proposed. In the present paper, we build upon this last approach and thus focus our attention on a strongly correlated model on

the triangular lattice. It was shown that on the mean-field level and near half-filling, a magnetically ordered CI with a very flat single-particle band emerges. Doping this nearly flat band to fractional fillings was shown to give rise to FCI states within the framework of an effective single-orbital model. Here, we give a detailed account of the mapping onto the effective single-orbital model and show how such topologically nontrivial and nearly flat bands emerge in Kondo-lattice and Hubbard models both for the limit of infinite onsite interactions and for more realistic intermediate interaction strength.

We then provide extensive numerical evidence, based on both eigenvalue spectra (e.g., ground-state degeneracy and spectral flow) and eigenstate properties (e.g., many-body Berry curvature and Hall conductivity), for the existence of FCI states in this model by using exact diagonalization. We discuss the robustness of FCI states against disorder originating from single-site defects in the magnetic ordering, which will always occur in realistic situations. Another very relevant issue in the context of FCI states is their competition with other phases,^{24,30} e.g. symmetry-broken states such as a charge-density wave (CDW). We study this issue by using a method that does not project onto the nearly flat Chern band and thus keeps the effects of dispersion. The model considered in this work allows for a careful study of the competition between finite dispersion and interactions. We map out a phase diagram for filling fractions $\nu = 1/3$ and $\nu = 2/3$. In the latter case, filling permits a commensurate CDW, whereas in the former it does not. The CDW is favored by Fermi-surface (FS) nesting, and we accordingly find the FCI at $\nu = 2/3$ to be far more stable when the bands are poorly nested.

This paper is organized as follows: in Sec. II, we extend the discussion of flat and topologically nontrivial bands arising in t_{2g} models and derive the effective model. Numerical results on the model are presented in Sec. III, where we first focus on information obtained from eigenenergies, namely gaps and flux insertion (Sec. III A) and fractional statistics of charged excitations in FCI states based on a recently introduced state-counting argument (Sec. III B).³¹ We then add information obtained from the eigenstates: the Hall conductivity, which allows us to address the impact of impurities in Sec. III D and the static charge-structure factor, which allows us to discuss the competition with the CDW at filling $\nu = 2/3$ in Sec. III E. We conclude with some remarks summarizing the main points in Sec. IV

II. TOPOLOGICALLY NONTRIVIAL AND NEARLY FLAT BANDS IN STRONGLY CORRELATED MULTI-ORBITAL SYSTEMS

In Ref. 41, it was shown that both e_g and t_{2g} orbital manifolds in octahedral coordination can reduce the bandwidth of topologically nontrivial bands. For a schematic illustration of orbital degeneracy in d -electron

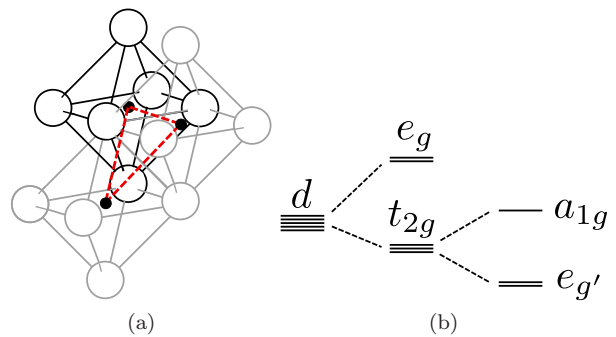


FIG. 1. (Color online) (a) Illustration of a triangular-lattice plane built of edge-sharing oxygen octahedra. (b) The five d orbitals of the transition-metal ion in the center are split into an e_g doublet and a t_{2g} triplet due to the local cubic symmetry; the latter is further split into one a_{1g} state and an e'_g doublet. (The splitting between the latter is exaggerated here for visibility.)

systems see Fig. 1. In particular, this was discussed for the spin-chiral phase arising in Kondo-lattice models on the triangular lattice^{14,42–44} at quarter and three-quarter fillings. While the flat band of interest mixes both the $3z^2 - r^2$ and the $x^2 - y^2$ orbitals in the e_g case, it is dominated by a particular orbital state in the t_{2g} manifold, the a_{1g} state, which allowed the straightforward mapping onto an effective one-band model.²² In this section, we first review the basic setup of the orbital symmetries in Sec. II A and the modifications of the hopping through the magnetic order in Sec. II B, as we believe that it may be of value to the reader. After this presentation of the physical ingredients at work here, we discuss how the nearly flat a_{1g} band arises due to effective longer-range hoppings. After the simplest scenario of infinite Hund's rule coupling in Sec. II C, we go to the more realistic multi-orbital model with finite interactions in Sec. II D, and finally decide on a relatively simple effective model in Sec. II E, which nevertheless captures several important features.

A. Impact of orbital symmetries on the one-particle Hamiltonian

In many transition-metal (TM) compounds, the local symmetry around a TM ion is cubic, with ligand oxygens forming an octahedron, as depicted in Fig. 1(a). This splits the degeneracy between the d levels, because the two e_g orbitals point toward the negatively charged oxygens, while the three t_{2g} levels have their lobes in between. Consequently, the energy of e_g levels is higher. Depending on the total electron filling, the valence states may be found in either manifold. We are here discussing the situation where the three t_{2g} levels share 2.5 to 3 electrons and the e_g levels are empty. Furthermore, we consider the case of a layered triangular lattice, as can be realized in compounds of the form ABO_2 .

In this geometry, the octahedra are edge sharing and electrons (or holes) can hop from one TM ion to its neighbor either through direct overlap or via the ligand oxygens. The hopping symmetries can be most easily worked out using the usual basis functions for the t_{2g} states, $|xz\rangle$, $|yz\rangle$, and $|xy\rangle$ ^{45,46} and following Refs. 47 and 48. Considering hopping for bonds along the \mathbf{a}_1 direction and choosing the local coordinate system such that this corresponds to the (1, 1) direction in the x - y plane, one finds that direct hopping t_d is only relevant for the xy orbital and conserves orbital flavor. Due to the 90° angle of the TM-O-TM bond, oxygen-mediated hopping t_0 is, on the other hand, mostly via the oxygen- p_z orbital and mediates processes between xz and yz states, thereby always *changing* orbital flavor. Hoppings along the other two, symmetry-related, directions \mathbf{a}_2 and \mathbf{a}_3 are obtained by symmetry transformations.

These hoppings can then be expressed in orbital- and direction- dependent matrix elements $t_{\mathbf{a}_k}^{\alpha,\beta}$, where α and β denote orbitals (xz , yz , and xy) and \mathbf{a}_k the direction. They are given by

$$\hat{T}_{\mathbf{a}_1} = \begin{pmatrix} t_{dd} & 0 & 0 \\ 0 & 0 & t_0 \\ 0 & t_0 & 0 \end{pmatrix}, \quad \hat{T}_{\mathbf{a}_2} = \begin{pmatrix} 0 & 0 & t_0 \\ 0 & t_{dd} & 0 \\ t_0 & 0 & 0 \end{pmatrix},$$

$$\hat{T}_{\mathbf{a}_3} = \begin{pmatrix} 0 & t_0 & 0 \\ t_0 & 0 & 0 \\ 0 & 0 & t_{dd} \end{pmatrix} \quad (1)$$

for NN bonds along the three directions \mathbf{a}_1 , \mathbf{a}_2 , \mathbf{a}_3 . The two hopping processes are expected to be of comparable strength, but with $|t_d| \lesssim |t_0|$ for $3d$ elements, and will typically have opposite sign.⁴⁶

If the width of a triangular layer made of octahedra is compressed (extended), the energy of the highly symmetric orbital state $|a_{1g}\rangle = (|xz\rangle + |yz\rangle + |xy\rangle)/\sqrt{3}$ is raised (lowered) with respect to the remaining orbital doublet (e'_g), see Fig. 1(b) for illustration. This energy shift can be written as

$$H_{JT} = -E_{JT}(n_{e_{g+}} + n_{e_{g-}} - 2n_{a_{1g}})/3 \quad (2)$$

and depends on the Jahn-Teller effect as well as on the lattice.⁴⁶ Especially for large splitting between a_{1g} and e'_g states, which may also be enhanced through onsite Coulomb interactions, see Sec. IID, it is more appropriate to use a basis that reflects the triangular lattice symmetry. We thus go over into the $(a_{1g}, e'_{g,1}, e'_{g,2})$ basis, which is done via⁴⁶

$$\begin{pmatrix} a_{1g} \\ e'_{g,1} \\ e'_{g,2} \end{pmatrix} = \hat{U} \begin{pmatrix} xz \\ yz \\ xy \end{pmatrix} = \frac{1}{\sqrt{3}} \begin{pmatrix} 1 & 1 & 1 \\ 1 & e^{i2\pi/3} & e^{-i2\pi/3} \\ 1 & e^{i4\pi/3} & e^{-i4\pi/3} \end{pmatrix} \begin{pmatrix} xz \\ yz \\ xy \end{pmatrix}. \quad (3)$$

The transformed hopping matrices $\tilde{T}_{\mathbf{a}_i}$ are then obtained from Eq. (1) as

$$\tilde{T}_{\mathbf{a}_1} = \hat{U}^\dagger \hat{T}_{\mathbf{a}_1} \hat{U} = \frac{1}{3} \begin{pmatrix} 3t_0 + \delta t & \delta t & \delta t \\ \delta t & \delta t & 3t_0 + \delta t \\ \delta t & 3t_0 + \delta t & \delta t \end{pmatrix},$$

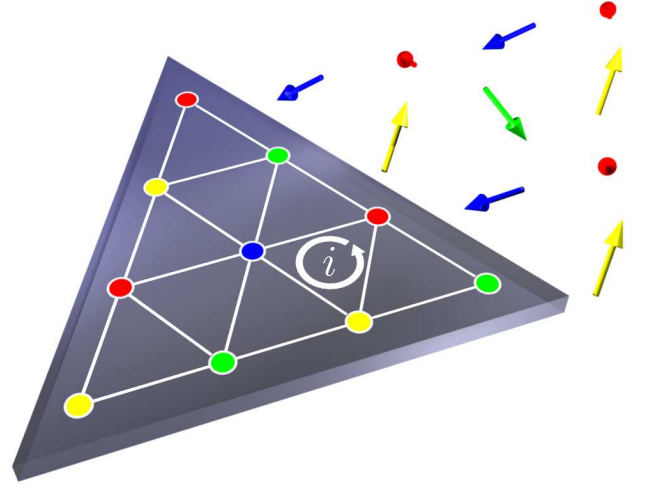


FIG. 2. (Color online) Illustration of chiral spin pattern and effective model including the magnetic texture as phase factors in hoppings.

$$\tilde{T}_{\mathbf{a}_2} = \hat{U}^\dagger \hat{T}_{\mathbf{a}_2} \hat{U} = \frac{1}{3} \begin{pmatrix} 3t_0 + \delta t & \delta t \omega & \delta t \omega^{-1} \\ \delta t \omega^{-1} & \delta t & (3t_0 + \delta t)\omega \\ \delta t \omega & (3t_0 + \delta t)\omega^{-1} & \delta t \end{pmatrix},$$

$$\tilde{T}_{\mathbf{a}_3} = \hat{U}^\dagger \hat{T}_{\mathbf{a}_3} \hat{U} = \frac{1}{3} \begin{pmatrix} 3t_0 + \delta t & \delta t \omega^{-1} & \delta t \omega \\ \delta t \omega & \delta t & (3t_0 + \delta t)\omega^{-1} \\ \delta t \omega^{-1} & (3t_0 + \delta t)\omega & \delta t \end{pmatrix}, \quad (4)$$

where $\delta t = t_{dd} - t_0$ and $\omega = e^{i2\pi/3}$. Observe that the intra-orbital hopping of the a_{1g} state is the same in all three lattice directions, as expected for a_{1g} symmetry. However, we also see that hopping elements mix all three orbitals.

B. Hopping topology through magnetic order: Berry phases

In addition to an orbital degree of freedom, we now consider coupling to a localized spin \mathbf{S}_i , modelled by a Kondo-lattice model, where the kinetic energy is given by hopping elements $t_{\mathbf{a}_k}^{\alpha,\beta}$ taken from the matrices Eq. (1) or Eq. (4). This situation is described by

$$\mathcal{H} = \sum_{\substack{\langle i,j \rangle \parallel \mathbf{a}_k, \sigma \\ \mathbf{a}_k, \alpha, \beta}} t_{\mathbf{a}_k}^{\alpha,\beta} c_{i,\sigma,\alpha}^\dagger c_{j,\sigma,\beta} - J_{\text{Kondo}} \sum_{i,\alpha} \mathbf{S}_i \cdot \mathbf{s}_{i,\alpha} \quad (5)$$

where $\langle i, j \rangle \parallel \mathbf{a}_k$ denotes NN bonds along the three directions \mathbf{a}_k , α and β are orbital indices, $c_{i,\sigma,\alpha}$ ($c_{i,\sigma,\alpha}^\dagger$) annihilates (creates) an electron with spin σ in orbital α at site i , and $\mathbf{s}_{i,\alpha}$ is the corresponding vector of orbital electronic spin operators. J_{Kondo} couples the itinerant electrons to a generic localized spin \mathbf{S}_i , the origin of which is left unspecified for the moment, but will be discussed extensively later. (It will turn out to be the spin degree

of freedom of the t_{2g} electrons themselves, as in Ref. 22.) The coupling is assumed to be FM, as one would expect from Hund's-rule coupling. However, we are furthermore going to consider \mathbf{S}_i as a *classical* spin, in which case AFM coupling to \mathbf{S}_i would lead to the equivalent results.

For classical spins and large J_{Kondo} , it is convenient to go over to a *local* spin-quantization axis, where “ \uparrow ” (“ \downarrow ”) refers to parallel (antiparallel) orientation of the electron's spin to the local axis. This simplifies the Kondo term to

$$H_{\text{Kondo}} = -J_{\text{Kondo}} \sum_{\mathbf{i}, \alpha} \mathbf{S}_i \cdot \mathbf{s}_{i, \alpha} = -J_{\text{Kondo}} \sum_{\mathbf{i}, \alpha} (n_{\alpha}^{\uparrow} - n_{\alpha}^{\downarrow}) / 2, \quad (6)$$

where n_{α}^{\uparrow} (n_{α}^{\downarrow}) is the electron density at site \mathbf{i} in orbital α with spin (anti-) parallel to the localized spin. This local spin definition is particularly convenient when going to the limit of large J_{Kondo} , where one immediately finds the low-energy states as given by only “ \uparrow ” electrons.

On the other hand, the fact that the spin-quantization axis is not the same at all sites implies that the hopping no longer conserves the new spin. Instead, hopping acquires as spin-dependent factor $t_{i,j}^{\alpha, \beta} \rightarrow t_{i,j}^{\alpha, \beta, \sigma, \sigma'} = t_{i,j}^{\alpha, \beta, \sigma, \sigma'}$,⁴⁹ with

$$u_{ij}^{\uparrow\uparrow} = c_i c_j + s_i s_j e^{-i(\phi_i - \phi_j)}, \quad (7)$$

$$u_{ij}^{\uparrow\downarrow} = c_i c_j + s_i s_j e^{i(\phi_i - \phi_j)}, \quad (8)$$

$$u_{ij}^{\bar{\sigma}\bar{\sigma}} = \sigma(c_i s_j e^{-i\sigma\phi_j} - c_j s_i e^{-i\sigma\phi_i}),$$

where $\bar{\sigma} = -\sigma$ and $c_i = \cos\theta_i/2$, $s_i = \sin\theta_i/2$ and the set of angles $\{\theta_i\}$ and $\{\phi_i\}$ are the polar and azimuthal angles corresponding to $\{\mathbf{S}_i\}$, respectively. As one can see, these effective hoppings can become complex, and it has been shown that non-coplanar spin configurations can endow the electronic bands with a non-trivial topology.^{13,14} Additionally, the itinerant electrons mediate an interaction between the localized spins, which typically competes with antiferromagnetic spin-spin interactions; on frustrated lattices, this competition can resolve itself in non-coplanar – and thus topologically nontrivial – phases.^{14,42–44}

C. Effective bands for a Kondo-lattice model with infinite Hund's rule coupling

The interplay of the orbital symmetries summarized in Sec. II A with the Berry phases of Sec. II B was discussed in Ref. 41 for the limit of infinite Hund's rule coupling to classical localized spins, corresponding to the double exchange model. In this case, one only keeps the \uparrow electrons parallel to the local spin-quantization axis and electrons effectively become spinless fermions. For the chiral spin pattern in Fig. 2, which has been found as the ground state of triangular Kondo-lattice models,^{14,42–44} the Berry phases between the four sites of the magnetic

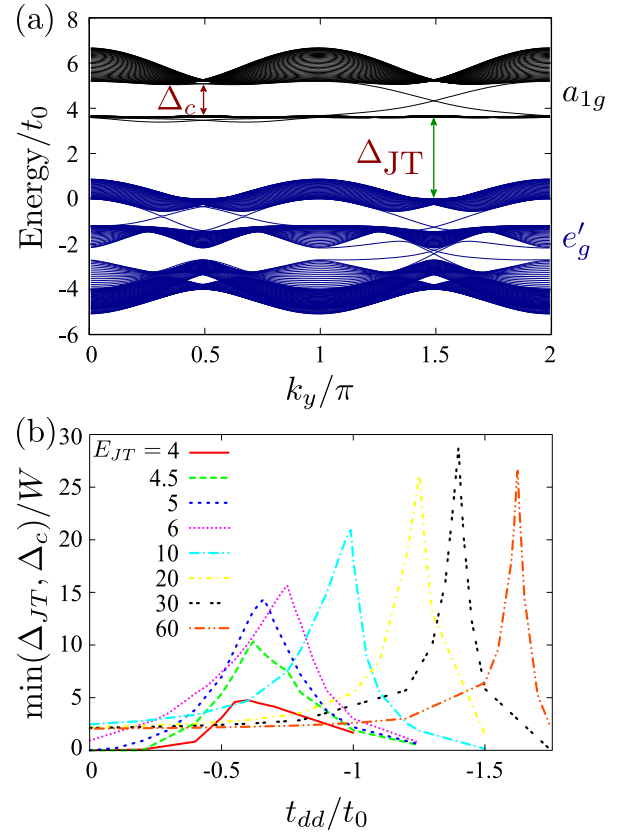


FIG. 3. (Color online) Flat lower chiral subband in the Kondo-lattice model with infinite Hund's rule coupling (double-exchange model). (a) Shows the one-particle energies of three t_{2g} orbitals coupled to localized spins, where the latter form a spin-chiral phase on a triangular lattice,^{14,42–44} see Fig. 2. The system is a cylinder, i.e., periodic boundary conditions along y -direction and open boundaries along x . The horizontal axis is the momentum in the direction with periodic boundaries. The gaps Δ_{JT} and Δ_c denote the gaps due to crystal-field splitting E_{JT} and to the chiral spin state. (b) shows the figure of merit M , see Eq. (10), for the lower a_{1g} subband. The curves for crystal-field splittings $E_{JT} = 4, 4.5, 5$ and 6 were already given in Fig. 3(b) of Ref. 22 and are repeated here for convenience.

unit cell can be parametrized as

$$u_{1,2}^{\uparrow\uparrow} = u_{3,4}^{\uparrow\uparrow} = \frac{1}{\sqrt{3}}, \quad u_{1,3}^{\uparrow\uparrow} = -u_{2,4}^{\uparrow\uparrow} = \frac{1}{\sqrt{3}} \quad (9)$$

$$u_{2,3}^{\uparrow\uparrow} = u_{4,1}^{\uparrow\uparrow} = -u_{3,2}^{\uparrow\uparrow} = -u_{1,4}^{\uparrow\uparrow} = \frac{i}{\sqrt{3}}.$$

It turns out that these hoppings can in fact be written in a two-site unit cell (containing sites 1 and 2) due to an internal symmetry of the four-site pattern,¹⁴ see also the effective model Eq. (23) below.

Combining the phases Eq. (9) with the hoppings given by Eqs. (1) or (4) and the crystal-field splitting Eq. (2) still gives a non-interacting model that can be easily solved in momentum space. One finds that large $|E_{JT}|$,

see Eq. (2), strongly reduces the dispersion of one subband.⁴¹ This can also be seen in Fig. 3(a), which shows the one-particle energies obtained on a cylinder. Figure 3(a) also reveals the edge states crossing some gaps, indicating the topologically nontrivial nature of these bands. Calculating Chern numbers C corroborates this and gives $C = \pm 1$.⁴¹ The band flatness can be expressed in terms of a figure of merit

$$M = \frac{\min(\Delta_{JT}, \Delta_c)}{W}, \quad (10)$$

where Δ_{JT} and Δ_c are the two gaps separating the narrow band of interest from the other orbitals and from the subband with opposite Chern number and W is the width of the narrow band. As has been pointed out,⁴¹ the lower subband can here become very flat, and as can be seen in Fig. 3(b), the flatness can be further improved by going to larger crystal fields and reaches values $M \approx 28$.

As these very flat bands can be achieved for large separation E_{JT} between the a_{1g} and e'_g states and as the band of interest then has almost purely a_{1g} character, it is natural to assume that one should be able to capture the most relevant processes with an effective a_{1g} model. (This is in contrast to the situation starting from e_g orbitals, where one finds intermediate E_{JT} to be optimal.⁴¹ In that case, the nearly flat bands can only be obtained if *both* orbitals contribute weight and one cannot easily reduce the situation to a one-band system.)

The impact of the e'_g levels on the effective a_{1g} dispersion can be taken into account in second-order perturbation theory. This includes processes where a hole hops from the a_{1g} orbital at site i to an e'_g state at j and back again to an a_{1g} state at a third site i' , which may or may not be the same as i . The denominator of these terms is the crystal-field energy E_{JT} and the numerator is obtained from the products $\tilde{T}_i^{ab}\tilde{T}_j^{ba} + \tilde{T}_i^{ac}\tilde{T}_j^{ca}$ (with a designating a_{1g} and b, c the e'_g states). In order to evaluate the second-order hopping between sites i and i' , these orbital hoppings have to be multiplied by the product of the Berry phases $u_{i,j}^{\uparrow\uparrow}$ and $u_{j,i'}^{\uparrow\uparrow}$ from Eq. (9) for all paths connecting i and i' via one intermediate site $j \neq i, i'$. Due to destructive interference, processes connecting NN and next-nearest neighbor (NNN) sites cancel while effective third-neighbor hopping, where there is only one path, remains. Since third-neighbor spins in the chiral phase are always parallel, the total Berry phase of this process is 1 in all directions, however, the hopping via a spin of different orientation in the middle reduces the hopping amplitude by $|u^{\uparrow\uparrow}|^2 = 1/3$, leading to

$$t_3 = -\frac{2(t_0 - t_{dd})^2}{27E_{JT}}. \quad (11)$$

A third-neighbor hopping $\propto \sum_i \cos 2\mathbf{k} \cdot \mathbf{a}_i$ turns out to have almost the same dispersion as the chiral subbands and can consequently almost cancel it in one subband. As its strength can be tuned by t_{dd} and E_{JT} , very flat subbands can be achieved, see Fig. 3(b).

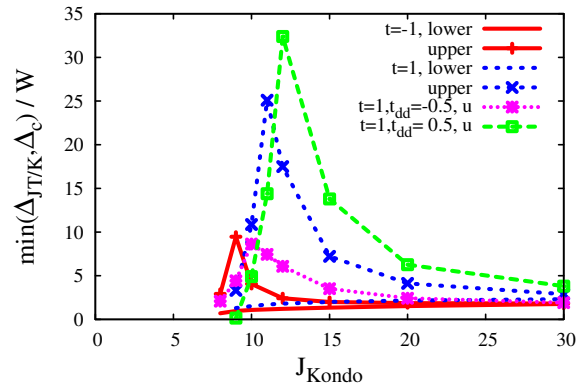


FIG. 4. (Color online) Figure of merit M , see Eq. (10), for finite Hund's-rule coupling J_{Kondo}/t_0 and $E_{JT} = 6t_0$. The bands designated as “upper” and “lower” refer to the two subbands of the a_{1g} states with spin parallel to the localized spin, which are separated by the gap opening in the spin-chiral phase, see Fig. 3(a).

D. Impact of the upper Kondo/Hubbard band: Flat bands for finite interactions

While the previous section has illustrated how one can understand the occurrence of nearly flat bands in a three-orbital double-exchange model, i.e., for infinite Hund's rule coupling to some localized spins, this section will discuss finite Hund's rule. Figure 4 shows the figure of merit for the band flatness Eq. (10) for a few sets of hopping parameters and for $E_{JT} = 6t_0$ depending on Hund's rule coupling J_{Kondo} to the localized spin, see Eq. (6). As can be seen in Fig. 4, the *upper* subband of the a_{1g} sector can now become nearly flat. (For $J_{\text{Kondo}} \gg |E_{JT}|$, one can of course still find flat lower subbands, as discussed above.)

The flatness of the upper subband can be explained by similar effective longer-range hoppings in second-order perturbation theory, this time also taking into account intermediate states with an electron in the upper Kondo band, i.e., with antiparallel spin. These additional terms can go either via the a_{1g} or via the e'_g orbitals and involve combined Berry phases of the form $u_{ij}^{\uparrow\downarrow}u_{ji'}^{\downarrow\uparrow}$. Again, one has to sum over all possible intermediate sites j and finds

$$t_1 = \frac{3t + \delta t}{3} + 2\frac{(3t + \delta t)^2}{9} \frac{1}{E_2} - 2\frac{\delta t^2}{9} \frac{1}{E_3}, \quad (12)$$

$$t_2 = 2\frac{(3t + \delta t)^2}{9} \frac{1}{E_2} - 2\frac{\delta t^2}{9} \frac{1}{E_3}, \quad (13)$$

$$t_3 = 2\frac{(3t + \delta t)^2}{27} \frac{1}{E_2} + 4\frac{\delta t^2}{27} \frac{1}{E_3} + 2\frac{\delta t^2}{27} \frac{1}{E_1}. \quad (14)$$

The NN, NNN and third-neighbor hoppings are here denoted by t_1 , t_2 , and t_3 . $E_1 = E_{JT}$, $E_2 = J_{\text{Kondo}}$, and $E_3 = J_{\text{Kondo}} - E_{JT}$ give the excitation energies of the intermediate states with (i) a hole in the e'_g states with spin parallel, (ii) an electron in the a_{1g} states with spin

anti-parallel and (iii) an electron in an e'_g state with spin anti-parallel. Like the bare NN hopping, these effective hopping-matrix elements acquire an additional Berry phase $u_{ii'}^\uparrow$ in the Hamiltonian, which only depends on the relative orientation of spins on the initial and final sites. NNN hopping t_2 via the upper Kondo band does not drop out, and NN hopping becomes renormalized.

The flat chiral subbands that have been observed in a three-orbital t_{2g} Hubbard model on the triangular lattice²² arise in situations similar to the finite- J_{Kondo} scenario, and a mapping to the Kondo-lattice model was shortly mentioned in the supplemental material of Ref. 22. The key point of the mapping is the observation that large crystal-field splitting E_{JT} , see (2), leads to an orbital-selective Mott insulator, where the e'_g levels are half filled and far from the Fermi level, while the states near the Fermi level have almost only a_{1g} character. The orbital degree of freedom is consequently quenched, because orbital occupations are already fully determined. A charge degree of freedom remains, as the a_{1g} orbital contains one electron per two sites. Charge fluctuations of the half-filled e_g levels, however, are suppressed due to the large Mott gap between their occupied and empty states. They can thus be described as a spin degrees of freedom, and the situation is further simplified, because they form a total spin with $S = 1$ due to Hund's rule. The a_{1g} electron is likewise coupled via FM Hund's rule to this spin. This situation – mobile carriers coupled via FM Hund's rule to localized spin degrees of freedom – is captured by a FM Kondo-lattice model.

These considerations can be cast in a more formal setting starting from the mean-field decoupling²² of the onsite Coulomb repulsion. The full interaction for equivalent t_{2g} orbitals reads

$$H_{\text{int}} = U \sum_{\mathbf{i}, \alpha} n_{\mathbf{i}, \alpha, \uparrow} n_{\mathbf{i}, \alpha, \downarrow} \quad (15)$$

$$+ (U' - J/2) \sum_{\mathbf{i}, \alpha < \beta} n_{\mathbf{i}, \alpha} n_{\mathbf{i}, \beta} \quad (16)$$

$$- 2J \sum_{\mathbf{i}, \alpha < \beta} (\mathbf{s}_{\mathbf{i}, \alpha} \cdot \mathbf{s}_{\mathbf{i}, \beta}) \quad (17)$$

$$+ J' \sum_{\mathbf{i}, \alpha < \beta} \left(c_{\mathbf{i}, \alpha, \uparrow}^\dagger c_{\mathbf{i}, \alpha, \downarrow}^\dagger c_{\mathbf{i}, \beta, \downarrow} c_{\mathbf{i}, \beta, \uparrow} + \text{H. c.} \right), \quad (18)$$

where $U = U' + 2J$ and $J' = J$ holds in the case of equivalent t_{2g} orbitals. We now concentrate on the regime of interest, where the a_{1g} orbital is separated from the e_g doublet by a sizable E_{JT} and does not have to be equivalent. As long as intraorbital interaction (15) and Hund's rule coupling (17) dominate over interorbital interaction (16) and crystal-field splitting (2), doubly occupied orbitals will be suppressed and the last term (18) will consequently not be important. Moreover, there is no reason for spins in different orbitals, but on the same site, to point in different directions, as the only interactions between spins are FM, i.e., we can use the same local quantization axis for all orbitals. In the case of doubly

occupied orbitals, one spin can be seen as lying antiparallel and as introduced in Sec. II B, “ \uparrow ” (“ \downarrow ”) denotes a spin parallel (antiparallel) to the local quantization axis. The corresponding mean-field decoupling is

$$H_{\text{mf}} \approx U \sum_{\mathbf{i}, \alpha} (\langle n_{\mathbf{i}, \alpha, \uparrow} \rangle n_{\mathbf{i}, \alpha, \downarrow} + n_{\mathbf{i}, \alpha, \uparrow} \langle n_{\mathbf{i}, \alpha, \downarrow} \rangle) \quad (19)$$

$$+ (U' - J/2) \sum_{\mathbf{i}, \alpha < \beta} (\langle n_{\mathbf{i}, \alpha} \rangle n_{\mathbf{i}, \beta} + n_{\mathbf{i}, \alpha} \langle n_{\mathbf{i}, \beta} \rangle) \quad (20)$$

$$- 2J \sum_{\mathbf{i}, \alpha < \beta} (\langle m_{\mathbf{i}, \alpha} \rangle m_{\mathbf{i}, \beta} + m_{\mathbf{i}, \alpha} \langle m_{\mathbf{i}, \beta} \rangle) + C, \quad (21)$$

where C is a constant²² and $m_{\mathbf{i}, \alpha} = (n_{\mathbf{i}, \alpha, \uparrow} - n_{\mathbf{i}, \alpha, \downarrow})/2$. Due to the last term (21), an electron in orbital β feels a FM coupling to a “classical localized spin” with length $\sum_{\alpha \neq \beta} \langle m_{\mathbf{i}, \alpha} \rangle$ that points along the local quantization axis. The axis can be parametrized by angles $\theta_{\mathbf{i}}$ and $\phi_{\mathbf{i}}$, which establishes the relation to Sec. II B. The first term (19) suppresses doubly occupied orbitals for all three orbitals. In the orbital-selective Mott-insulator, $n_{\mathbf{i}, \alpha} \approx n_{\mathbf{i}, \alpha, \uparrow} \approx 1$ for the e'_g states. The second term (20) thus mainly enhances the effect of $E_{\text{JT}} \rightarrow E_{\text{JT}} + 2U' - J$. The last term (21) becomes equivalent to the Kondo term, Eq. (6):

$$H_{\text{Kondo}, a_{1g}} = -2J \sum_{\mathbf{i}} m_{\mathbf{i}, a_{1g}} = -J \sum_{\mathbf{i}} (n_{\mathbf{i}, a_{1g}, \uparrow} - n_{\mathbf{i}, a_{1g}, \downarrow}). \quad (22)$$

Finally, we note that the fact that onsite interactions U and J are only large, but *not* infinite, is important for the spin-chiral ground state: for very large U and J , the ground state becomes a ferromagnet.²² This can be related to the fact that the Kondo-lattice model requires either finite J_{Kondo} ⁴² or additional AFM inter-site superexchange⁴³ to support a spin-chiral instead of a FM state. At finite onsite interactions, virtual excitations with doubly occupied e'_g orbitals are possible and lead to second-order processes that are similar to the effective longer-range hoppings discussed above. In such a process, an e'_g electron hops into an occupied e'_g state at a NN site, creating a (virtual) intermediate state with energy $\propto U + J \approx U' + 3J$, and hops back in the next step. Such a process yields an energy gain $\propto t_{e'_g}^2 / (U + J)$ and is only possible if the spins of the two involved electrons, which occupy the same orbital in the intermediate state, are opposite. The mechanism thus effectively provides the needed AFM intersite superexchange and the spin-chiral state becomes stable for wide parameter regimes, including ranges supporting nearly flat upper chiral subbands.²²

E. Effective Model

As we have discussed in the previous Sec. II D, the most realistic route to nearly flat bands with nontrivial

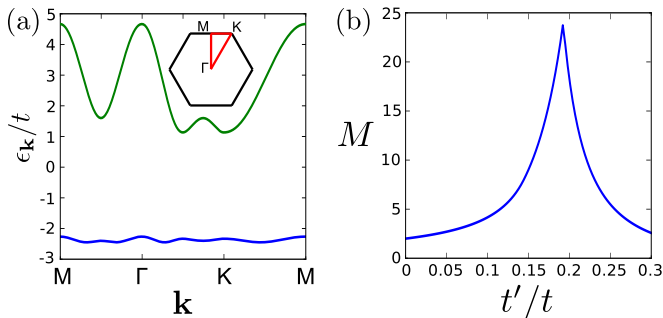


FIG. 5. (Color online) (a) Energy dispersion $e_{\mathbf{k}}$ for $t'/t = 0.2$. The inset shows the path taken through the first Brillouin zone. (b) Flatness ratio M , see Eq. (10), as a function of t'/t . The flatness ratio has been calculated from the dispersion along the high-symmetry directions shown in the inset on the left.

topology on the triangular lattice arises at finite Hubbard/Kondo coupling, where effective second-neighbor hopping is generated in addition to NN and third-neighbor terms. However, we have found that all essential features of the band structure can be captured by using just NN and third-neighbor hoppings (see Figure in the supplemental material of 22). In the interest of simplicity, we consequently adopt here the kinetic energy

$$H_{\text{kin}}(\mathbf{k}) = 2t \sum_j \sigma^j \cos \mathbf{k} \cdot \mathbf{a}_j + 2t' \sum_j \sigma^0 \cos 2\mathbf{k} \cdot \mathbf{a}_j, \quad (23)$$

where \mathbf{a}_j ($j = 1, 2, 3$) denote the unit vectors on the triangular lattice, and t and t' are the NN and third-neighbor hopping, which can be related to Eqs. (9) and (11) for the double-exchange scenario, to Eqs. (12) and (14) for finite onsite interactions, or which can be taken as fit parameters. Pauli matrices σ^j and unit matrix σ^0 refer to the two sites of the electronic unit cell in the chiral state.¹⁴ The unit cell and the topologically non-trivial bands are due to the symmetry breaking involved in the underlying magnetic order. The dispersion of Eq. (23) is

$$\epsilon_{\mathbf{k}}^{\pm} = \pm 2t \sqrt{\sum_j \cos^2 \mathbf{k} \cdot \mathbf{a}_j} + 2t' \sum_j \cos 2\mathbf{k} \cdot \mathbf{a}_j. \quad (24)$$

From now on, we use the effective NN hopping t as unit of energy; the band flatness can then be tuned by varying the ratio t'/t .

The longer range hopping t' determines the flatness of the bands of H_{kin} , which can be expressed by the figure of merit M , see Eq. (10). Figure 5 shows M depending on t' , and one sees that ratios $M \gtrsim 20$ can be reached for $t' \approx 0.2$. Such flatness ratios can reasonably be achieved in the low-energy bands of a strongly correlated t_{2g} system on a triangular lattice.²² Changing the sign of t' simply mirrors the dispersion vertically, i.e., it is then the upper band that becomes nearly flat. When going away from maximal M , the bands for smaller and larger t' differ

qualitatively; for $t' < 0.2$, the Fermi surface (FS) at some fillings is almost perfectly nested. We are going to discuss the impact of these differences in Sec. III E.

The NN Coulomb interaction

$$H_{\text{int}} = V \sum_{\langle i,j \rangle} n_i n_j, \quad (25)$$

is added to the kinetic term (23), giving the total Hamiltonian $H = H_{\text{kin}} + H_{\text{int}}$. While the spin-chiral phase providing the nontrivial topology can only be expected to remain stable for not-too-large V and doping of the flat band, we are going to study a variety of filling and interaction ranges to obtain a comprehensive picture of the model on finite-size systems.

III. RESULTS

The interacting Hamiltonian can be diagonalized exactly for small systems, using the Lanczos method.^{50,51} Unless otherwise noted, the results presented here are on a 4×3 unit-cell torus (i.e., 4×6 real-space sites). We do not project onto the flat subband, see Fig. 5(a), but instead model the whole system of both subbands with $C = \pm 1$. While this approach increases the Hilbert space and thus restricts system size, it has the advantage that competition with phases mixing the two subbands is included automatically. We use several observables to detect FCI states and to distinguish them from other phases; first, we discuss conclusions to be drawn from the eigenvalues, and later also include information obtained from the eigenstates, namely the many-body Chern number as a topological invariant and the charge-structure factor indicating formation of a (conventional) charge-density wave.

Even though the results of our investigation do not allow for conclusive finite-size scaling, we have verified that the findings presented here are consistent for smaller as well as somewhat larger systems. Furthermore, the main features of the FCI states found are consistent for all aspect ratios yielding the same system size, apart from those that reduce the system to a one-dimensional chain. Before passing, we note that we have obtained similar results to the ones presented here for several other filling fractions $\nu = p/q$, with $q = 5, 7$. Conclusive evidence for $4/5, 5/7, 6/7$ states could not be obtained, in agreement with reported results for another model.²⁴

A. Eigenvalues and flux insertion

FCI states manifest themselves in features of the obtained eigenvalue spectra. Traditional FQH ground states are q -fold quasi-degenerate on a finite torus at filling $\nu = p/q$.⁵² The same degeneracy is expected to occur for FCI states as well, at least within certain well-defined limits.³¹ Quasi-degenerate FQH ground-state eigenvalues

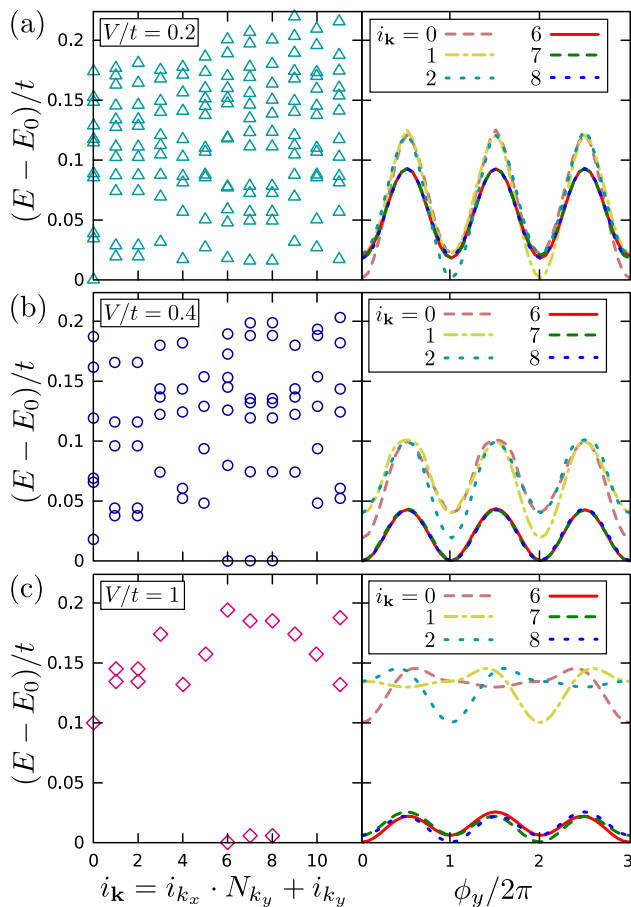


FIG. 6. (Color online) Eigenvalue spectrum and evolution of selected levels under flux insertion for different values of V/t . In all panels $t'/t = 0.2$.

must also exhibit spectral flow, leading each of them into another upon insertion of a flux quantum.⁵³ Magnetic fluxes can be modelled by introducing phase factors to the hopping from site $\mathbf{i} = i_x \mathbf{a}_1 + i_y \mathbf{a}_2$ to site $\mathbf{j} = j_x \mathbf{a}_1 + j_y \mathbf{a}_2$, thus leading to the transformation $t_{\mathbf{i},\mathbf{j}} \rightarrow t_{\mathbf{i},\mathbf{j}} \exp \left[i \left(\phi_x \frac{j_x - i_x}{L_x} + \phi_y \frac{j_y - i_y}{L_y} \right) \right]$. In this manner, an electron hopping around the lattice in the x/y direction picks up a phase $\phi_{x/y}$.

The features described above are illustrated, as a function of V/t , in Fig. 6 for $\nu = 1/3$. In this case, the three quasi-degenerate ground states emerge from the continuum as the interaction strength is increased. Insertion of one flux quantum indeed leads from one ground-state eigenvalue to another. It can also be seen that spectral flow is a general property of the eigenvalue spectrum, and we have found that it also occurs even at $V/t = 0$. The $\nu = 2/3$ ground states behave in a similar fashion. It can be seen that the FCI states remain gapped for a range of both M and V . In order to define a physically meaningful phase boundary, however, one has to make sure that the ground states remain gapped upon flux insertion, not only in their own momentum sector, but also

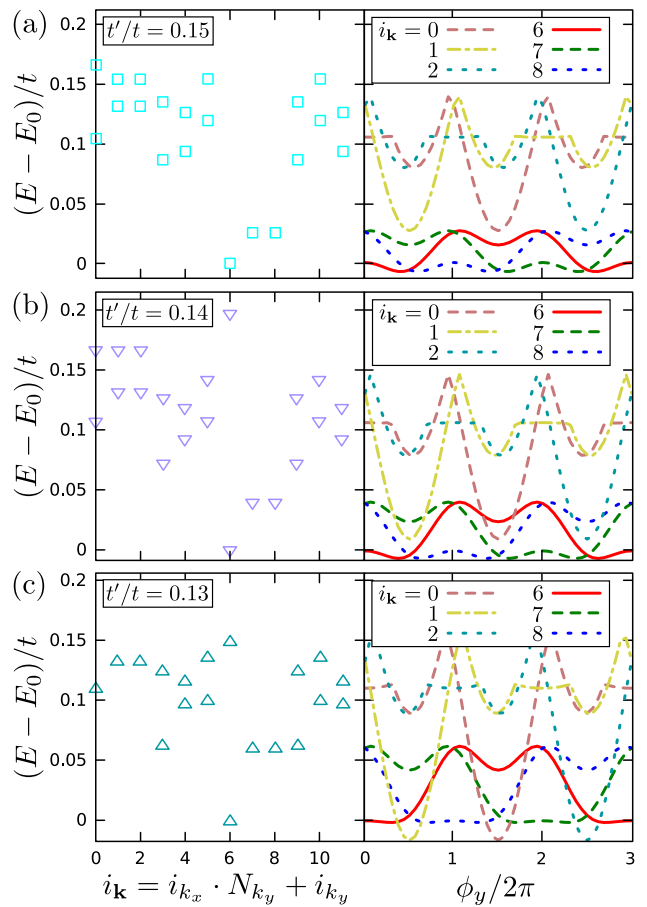


FIG. 7. (Color online) Eigenvalue spectrum and evolution of selected levels under flux insertion for different values of t'/t . In all panels $V/t = 1$.

across momentum sectors. The reason is that the presence of impurities would mix the momentum sectors and therefore close the gap if the quasi-degenerate FCI-state levels cross excited-state levels.

As seen in Fig. 6, interaction mostly changes the energy differences between groups of three quasi-degenerate eigenstates, which flow into each other upon flux insertion, and has less impact on the energy splitting within each manifold. When tuning the transition via increasing the band dispersion, the situation is somewhat different, see Fig. 7. For $M \approx 10$, the FCI ground state is destroyed by increasing the split between quasi-degenerate levels, permitting a higher-energy states to mix with the FCI-state manifold for some flux values. The splitting between ground states in the traditional FQHE case is due to quasiparticle-quasihole excitations propagating around the torus and therefore depends mainly on system size, becoming zero in the thermodynamic limit.⁵² In the finite tight-binding lattice systems discussed here, the splitting is affected significantly by the residual kinetic energy of the partially filled band, as can be seen in Fig. 7. Since the dispersion is present also in the thermodynamic limit, it is not clear whether the splitting

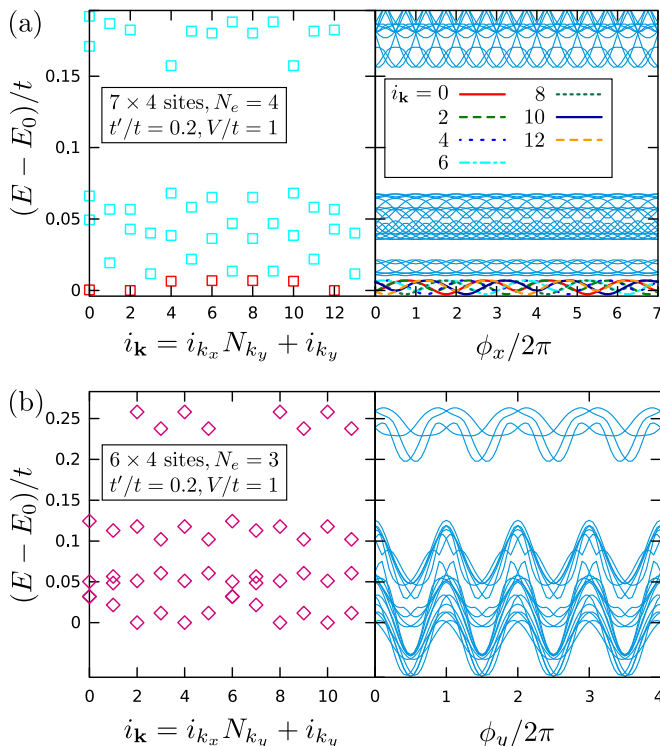


FIG. 8. (Color online) Eigenenergy spectrum and spectral flow for FCI state with quasiholes introduced (a) by enlarging the system or (b) by removing particles. The numbers of levels below the legends are (a) 35 and (b) 40 respectively, in agreement with the counting rule of Ref. 31. In the 7×2 -unit cell system, the filling fraction is $\nu = 2/7$. There are seven quasi-degenerate ground states (marked in red), which are slightly separated from the rest of the states in the low-energy sector and exhibit spectral flow (shown in different colors). Their Chern number is $C = 2/7$ within the numerical error margin.

survives to the thermodynamic limit or not in this system.

Despite level rearrangements or increasing spread between eigenvalues, FCI states remain topologically conjugate upon varying the band flatness or the interaction strength. A factor that can split this conjugacy is disorder, as will be shown in the Sec. III D. At the same time, ground-state levels that remain gapped upon flux insertion along one direction may cross excited-state levels upon flux insertion along another direction. A more careful analysis, based both on eigenenergy as well as on eigenstate properties, is necessary to uniquely determine a gapped ground state for a given parameter set. This is the purpose of Sec. III C. Before investigating eigenstates, however, the next section is going to discuss another aspect of eigenenergies, fractional statistics.

B. Fractional statistics

The concept of generalized Pauli principles,⁶ according to which states with clustered anyonic quasiparticles are energetically penalized, has served as a tool to indicate fractional statistics in FQH states.^{54,55} As was first demonstrated heuristically²⁰ and later on substantiated theoretically,³¹ the same logic holds for FCI states. For the $\nu = 1/3$ FCI state, the number of quasihole-state levels in a well separated, low-energy Fock space is equal to the number of (1,3)-admissible partitions of the momentum sectors on the torus. The individual states per momentum sector can also be accounted for, due to an emergent translational symmetry (see Ref. 31 for details). This symmetry is a characteristic feature of all the FCI states we have found in the triangular lattice model. In this section, we demonstrate that quasihole states of the triangular-lattice model obey the same state-counting arguments.

Quasiholes can be introduced in a FCI state by either removing electrons or increasing the system size. An example of both cases is presented in Fig. 8. The counting rule is verified in both cases. The counting rule can also be easily generalized to all Laughlin filling fractions $\nu = 1/q$ and we have verified it for $\nu = 1/5$ in this model.

Apart from the agreement to the counting rule, one can also notice the emergence of a “daughter” FCI state within the gapped low-energy sector, as expected in the hierarchy picture. Even though in the present context this is mainly a peculiarity of the small system sizes, it can nevertheless be viewed as a simple example of the formation of a hierarchical FCI state among the quasiparticle states of a “parent” FCI state. Taking this observation one step further, it can be seen that the spectrum looks qualitatively different under flux insertion in the two cases presented in Fig. 8, namely, the eigenvalue spectrum in the case where the filling is $\nu = 1/4$ looks more like that of the non-interacting system with levels crossing upon flux insertion, whereas at $\nu = 2/7$ levels come in small groups, which remain separated under flux insertion (compare to Fig. 6). This observation can be compared to the composite fermion theory of the FQHE,⁵⁶ according to which the state of a FQH system at filling fractions with even denominators can be effectively described by free fermions with flux tubes attached to them. This composite-fermion view of the FCI hierarchy of states has also been supported by recent numerical calculations.²⁴ These two different facets of the same model can serve as an example of the compatibility between the hierarchy and composite-fermion pictures of the FQHE in an unconventional FQH system.

C. Topological invariant

The most unambiguous characteristic of a FCI state is arguably its Hall conductivity. The ground-state Hall conductivity of a FCI at filling $\nu = p/q$ should be exactly

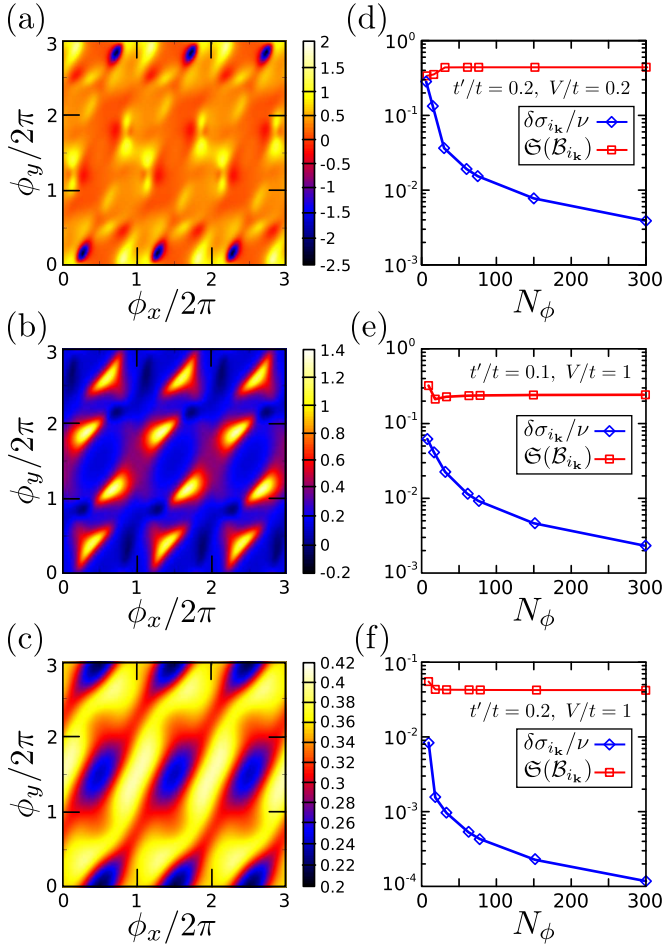


FIG. 9. (Color online) (a-c) Berry curvatures \mathcal{B}_{i_k} , (d-f) their standard deviations $\mathfrak{S}(\mathcal{B}_{i_k})$ from the exact average and relative deviations of Hall conductivities $\delta\sigma_{i_k}/\nu$ as a function of grid size for the state $i_k = 6$, when it is in the excited-state quasi-continuum (top) and in the ground-state manifold (middle and bottom). The integrations in Eq. (26) have been approximated by simple Riemann sums. N_ϕ is the number of $\phi_{x/y}$ points taken in the range $[0, 6\pi)$ in each direction.

ν . Occasionally, this quantity is referred to as “fractional Chern number”, to highlight the connection to the topological aspects of FCI states. The Hall conductivity σ of a gapped, degenerate state, measured in units of e^2/h in the following, can be efficiently calculated using the Kubo formula:^{57,58}

$$\sigma = \frac{N_c}{\pi q} \sum_{n=1}^q \iint_0^{2\pi} d\phi_x d\phi_y \mathfrak{S} \sum_{n' \neq n} \frac{\langle n | \frac{\partial H}{\partial \phi_y} | n' \rangle \langle n' | \frac{\partial H}{\partial \phi_x} | n \rangle}{(\epsilon_n - \epsilon_{n'})^2}, \quad (26)$$

where N_c is the number of unit cells, $|n\rangle$ are the q -fold degenerate many-body ground states and $|n'\rangle$ are higher-energy eigenstates. The corresponding eigenenergies are $\epsilon_{n/n'}$. The $\phi_{x/y}$ dependence of the Hamiltonian comes from magnetic fluxes going through each of the handles of the torus, as discussed in Sec. II E.

The integrand in Eq. (26) is proportional to the Berry

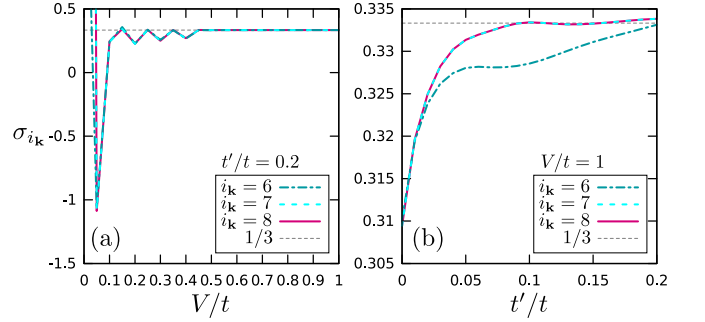


FIG. 10. (Color online) Hall conductivity, see Eq. (26), for each of the three quasi-degenerate FCI states as a function of (a) the interaction strength V/t and (b) the third-neighbor hopping t'/t (right). Note the different scales on the vertical axes.

curvature \mathcal{B}_n for each of the states in the degenerate ground state. For FCI states, Berry curvatures are periodic functions varying with $\phi_{x/y}$. In Fig. 9, the many-body Berry curvature for a specific state, which develops into one of the FCI ground states, is shown. It is seen that its smoothness varies as this state emerges from the excited state continuum. The period extends over q flux quanta in one direction and one flux quantum in the other, remains unchanged for all values of V and it is the same for all states in the ground-state manifold. The Berry curvature of the other two ground states is the same function, but translated by one and two flux quanta in the ϕ_y direction respectively. Even when the many-body Berry curvature of a FCI state is strongly varying, it is often centered around the value corresponding to the filling fraction and, since it is periodic, the Hall conductivity obtained by integration is very close to the quantized value. This occurs even if the FCI state is not a ground state. In the example presented in Fig. 9, the Hall conductivity is in all three cases equal to $\nu = 1/3$ within the numerical accuracy, which we will now discuss.

The Hall conductivities we have calculated are very close to the expected exact values in the FCI regime, despite the fact that the integrations involved are performed numerically. The relative deviation with respect to the exact value for the case of $\nu = 1/3$ is presented in Fig. 9. This example illustrates that the error in the Hall conductivity due to the finite size of the system should be smaller than 1%, at least for the Kubo formula approach, even for small systems. In the case of clearly gapped FCI ground states, the accuracy is even better, due to the integrand being very smooth. In all cases, we have used simple Riemann summation to evaluate integrals, in order to obtain upper bounds for the numerical errors. Other methods, like the Simpson rule, would converge for smaller grid sizes. It should be noted that when the Hall conductivity of an individual state within the degenerate ground state is evaluated, the integration should be extended over the whole period of the Berry curvature. This is no longer necessary when calculating

the average Hall conductivity and the integration range can then be restricted to $[0, 2\pi)^2$.

The effects of interaction and band dispersion can also be traced in the behavior of the Hall conductivity. This is shown in Fig. 10. Outside the FCI regime, where low-energy levels cross upon flux insertion, the Hall conductivity oscillates. It converges to ν at about the value of V/t for which the FCI states separate from the excited-state spectrum, forming a three-fold degenerate ground state. On the other hand, the Hall conductivity of these states remains close to $1/3$ with deviation from the flat-band limit, and only changes smoothly with t'/t , converging to the expected value close to the phase boundary discussed in Sec. III E.

D. Disorder

FQH states must be robust against disorder, as long as the energy scale of the disorder is smaller than the gap.⁵² The magnetic texture in the three-orbital model presented is generated spontaneously by itinerant electrons, so an expected source of disorder are local inhomogeneities in the chiral spin pattern. A simplistic approach to simulate this effect is to vary the flux picked up by an electron hopping along one selected bond of the finite cluster. This is done by varying the phase φ in the phase factor in front of the corresponding hopping. The effect of such a variation on Hall conductivities at $\nu = 1/3$ is shown in Fig. 11.

As long as the energy scale of the disorder is small enough, the ground states remain separated by a gap from the rest of the spectrum and their average Hall conductivity remains constant. The Hall conductivities of the individual quasi-degenerate ground states are not smooth functions of magnetic disorder. In particular, as soon as the impurity is switched on, the Hall conductivity of each individual state jumps to an integer value. Also, Berry curvatures are no longer smooth functions of $\phi_{x/y}$. Nevertheless, the Hall conductivities are still numerically well defined, as demonstrated in the right panels of Fig. 11, and their average, which is the proper observable quantity in the thermodynamic limit, remains constant as the disorder is varied. This invariance of the Hall conductivity directly demonstrates the topological robustness of FCI states.

Again in analogy to FQH states,⁵⁹ disorder introduces further splitting, apart from the one due to dispersion discussed in Sec. III A, between FCI ground-state eigenvalues, which no longer exchange places under flux insertion. This splitting is expected to be a finite-size effect and should disappear in the thermodynamic limit. A conclusive proof of this statement is however beyond the scope of this work. Despite the similarities, the impact of disorder in general on the energy-scale balance necessary for FCI states is qualitatively different than the situation in traditional FQH states. For example, disorder may have a different effect depending on the in-

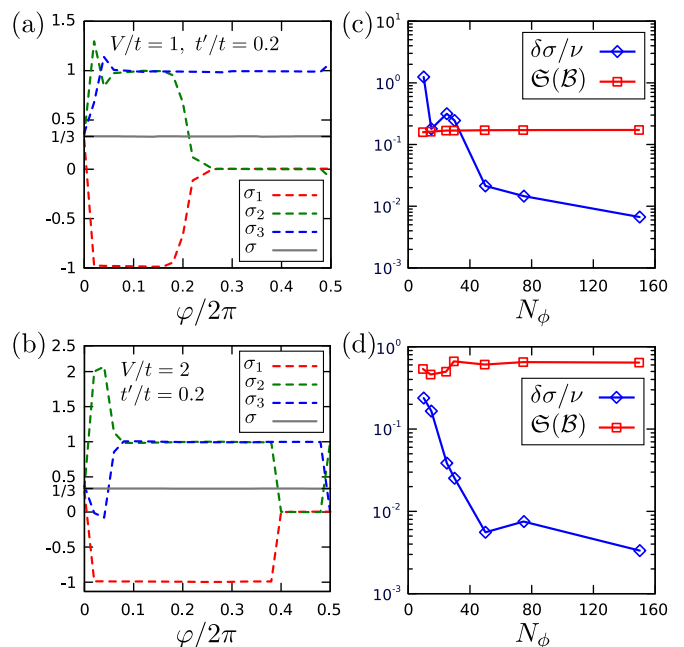


FIG. 11. (Color online) (a,b) Hall conductivities of the three lowest-energy states and their average as a function of disorder phase φ . (c,d) Standard deviation $\mathfrak{S}(\mathcal{B})$ of total Berry curvature \mathcal{B} , defined by adding up the many-body Berry curvatures \mathcal{B}_n of the three lowest-energy states for each value of $\phi_{x/y}$, and relative deviation $\delta\sigma/\nu$ of Hall conductivity as a function of grid size. N_ϕ is the number of $\phi_{x/y}$ points taken in the range $[0, 2\pi)$ in each direction. The results shown in the right panels are for $\varphi \simeq 2\pi/3$, but are qualitatively the same for all other values of φ .

teraction strength and range, and may lead to another, possibly topologically trivial, state, as has been shown in a recent study on the checkerboard lattice involving chemical-potential disorder.⁶⁰

E. Competition with Charge-density wave and Phase diagram

Early on, it was pointed out that an important prerequisite for the emergence of a FCI state is the balance between three energy scales, namely the width of the topologically non-trivial band, the gap(s) separating it from other bands and the Coulomb interaction strength.^{15–18} If the ratio between the first two, as expressed by the figure of merit Eq. (10), is large, then the interaction can become strong enough to induce FCI states, but remain small compared to the band gaps, which avoids mixing in wave function of different topological character. Many investigations have been focused on models in the perfectly flat band limit (exactly as in a Landau level), supplemented by various types of interaction. Rather recently, it was reported that the band flatness alone is not in fact a reliable indicator for the stability of FCI states.³⁰

In this section, we discuss how a finite dispersion in-

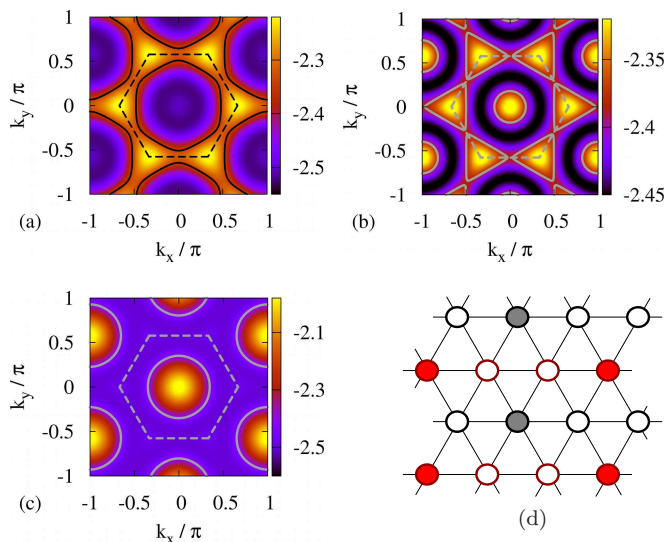


FIG. 12. (color online) Dispersion (gray-/ color-scale) and Fermi surface (FS) for $\nu = 2\bar{n} = 2/3$ (thick solid line) for (a) $t'/t = 0.16$ and $M = 11.16$, (b) $t'/t = 0.19245$ and $M = 24$ (very close to maximal M) and (c) $t'/t = 0.25$ and $M = 5.5$. Dashed lines indicate the first Brillouin zone. (d) illustrates the CDW possible for $\nu = 2\bar{n} = 2/3$. Black and red/gray circles indicate the two sublattices of the spin-chiral order and the effective model Eq. (23), filled circles the particles in the CDW state induced by large V/t .

fluences the stability of FCI states in a triangular-lattice model, where we focus on band filling and FS nesting. The first presents a rather obvious difference to LLs, as has recently also been mentioned in Ref. 24: while a LL is expected to be particle-hole symmetric, the nearly flat subband of a lattice model is not. We are going to discuss filling fractions $\nu = 1/3$ and $\nu = 2/3$ that turn out to clearly exemplify this difference. The latter case, which was also shortly discussed in Ref. 22, corresponds to $1/3$ filling of the original triangular lattice, where NN Coulomb interaction can stabilize a CDW [with particles at second-neighbor sites, see Fig. 12(d)], while no such CDW is possible at $\nu = 1/3$. The competition between the FCI and the CDW is in turn strongly affected by FS nesting, and we are going to see that the FCI is far more stable for more dispersive bands without nesting than for flatter bands with a nested Fermi surface. However, we are also going to see that very flat bands allow for FCI states at the lowest interaction strengths, even though they are in our case very well nested.

As mentioned in Sec. II E, varying t'/t allows us to tune the band flatness and to moreover switch between regimes with and without FS nesting. Examples are shown in Fig. 12, where the dispersion as well as the Fermi surface corresponding to $\nu = 2/3$ are shown for some values of t'/t . Both for near-optimal $t'/t = 0.19245$ ($M = 24$) and for smaller $t'/t = 0.16$ ($M \approx 11$), the FS contains hexagons with almost perfectly nested segments. A difference between the two cases is on one hand

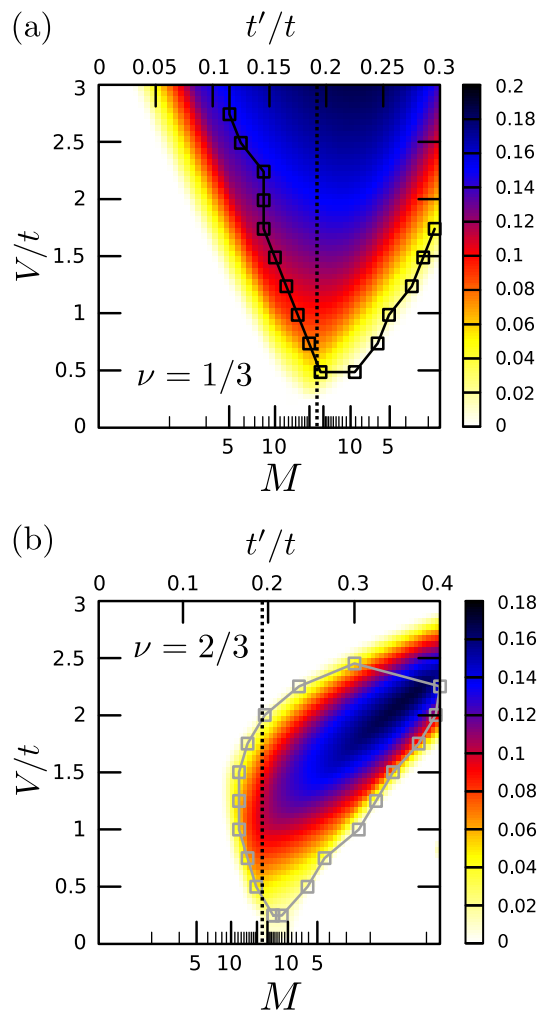


FIG. 13. (Color online) Gap of three-fold degenerate FCI ground state as a function of M and V/t , for (a) $\nu = 1/3$ and (b) $\nu = 2/3$, shown in colorcode. The dashed lines indicate the phase boundary, defined by the condition that the gap remains open for all values of inserted magnetic flux. The flatness ratio M of the flat band of H_{kin} (bottom scale) is adjusted by varying t'/t (top scale). The maximum value of the flatness ratio ($M \simeq 24$) is marked by the dotted lines.

the flatness ratio, but on the other hand, the flatter bands also have an additional circular FS around the Γ point. For $t'/t \gtrsim 0.23$, only the circular FS remains (see the example with $t'/t = 0.25$ and $M = 5.5$) and there is thus no longer good nesting.

Figure 13 shows the region where FCI states are stable on a 24-site (4×3 unit-cell) system, as a function of Coulomb interaction strength V and the flatness ratio M , which is in turn controlled by third-neighbor hopping, see Fig. 5. The two panels are for fillings $\nu = 1/3$ and $\nu = 2/3$. In both cases, the ground-state manifold in the FCI state is expected to be three-fold degenerate. The colorcode indicates the gap between the three ground states and the fourth lowest eigenstate in the absence of applied magnetic flux. In order to define a physically

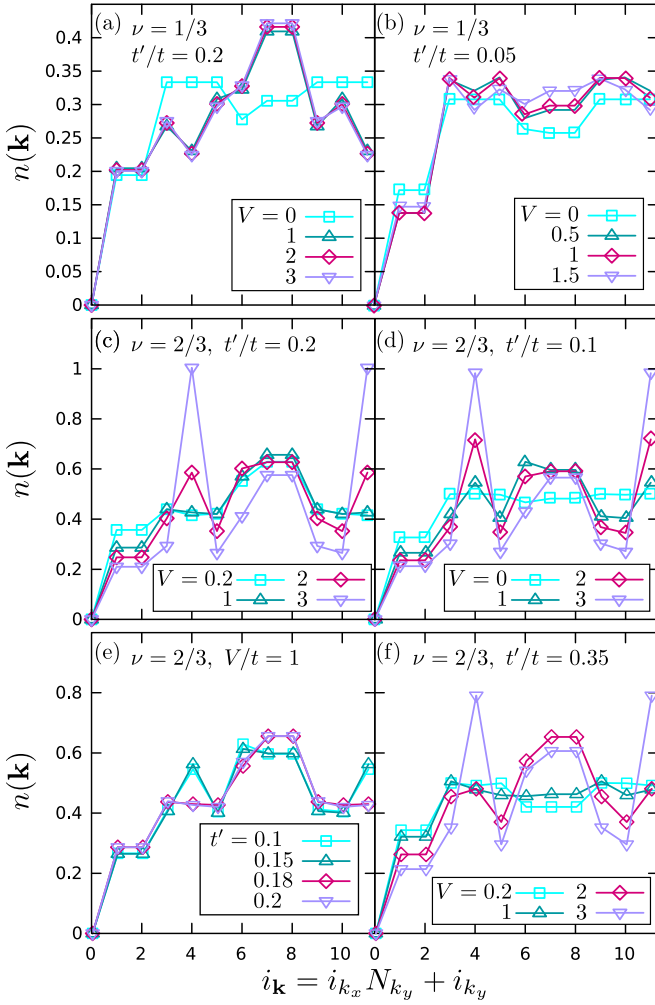


FIG. 14. (Color online) Static structure factor for various values of t'/t and V/t at filling fractions (a,b) $\nu = 1/3$ and (c-f) $\nu = 2/3$. The sharp peaks indicate the formation of a charge-ordered state. In the FCI regime, the static structure factor of all three quasi-degenerate ground states is identical.

meaningful phase boundary, however, one has to make sure that the ground states remain gapped upon flux insertion, not only in their own momentum sector, but also across momentum sectors, see Sec. III A. The solid lines in Fig. 13 indicate the phase boundary determined by taking these considerations into account. We have verified that the phase diagrams obtained from a 30-site torus are qualitatively the same as the ones shown here. The stability range of the FCI differs for $\nu = 2/3$ and system sizes commensurate with the CDW (3×6 and 6×6 sites), but the corresponding phase-diagram area is still finite.

For both fillings, the system is in a metallic state at small V/t , while finite values of V/t can lead to FCI ground states for an extended range of the band flatness. In the case of $\nu = 1/3$, the FCI state can be induced for any band dispersion by making V large enough. The FCI persists even for V/t considerably larger than the band gap. This has also been observed for another FCI model

on the checkerboard lattice,¹⁸ and appears to indicate that the fermions are dilute enough to occupy mostly one subband regardless of V/t , so that a mixing of the topological character of the two bands does not occur. In contrast, the $\nu = 2/3$ FCI states survive only for moderate values of V/t . Larger interaction strengths lead to a different ground state, which is, as we will argue below, a CDW.

To determine the type of order in each of the regions in Fig. 13, we calculate key properties of the corresponding ground states. The FCI states, despite the hints from the energy spectrum, have to be identified by their topological invariant, see Sec. III C. To find out whether there is tendency towards charge order in the rest of the phase diagram, we calculate the static (charge-)structure factor (SSF), defined as:

$$n(\mathbf{k}) = \frac{1}{N_s} \langle 0 | \sum_{j,l} e^{i\mathbf{k} \cdot (\mathbf{R}_j - \mathbf{R}_l)} (\hat{n}_j - \bar{n})(\hat{n}_l - \bar{n}) | 0 \rangle, \quad (27)$$

where N_s is the number of sites, \hat{n}_j is the electron-number operator acting on the site at position \mathbf{R}_j , $\bar{n} = \nu/2$ is the average electron number and $|0\rangle$ stands for the many-body ground state. Charge-density modulations are marked by sharp features in $n(\mathbf{k})$ at certain wave vectors. Liquid states, on the other hand, should be featureless in comparison to charge-modulated states.

Even though the accessible system sizes are not large enough to exemplify the featurelessness of liquid states, a qualitative difference between liquid and charge-modulated states can be seen. Examples are shown in Fig. 14. At $\nu = 1/3$ and within the FCI regime, $n(\mathbf{k})$ remains almost unchanged upon variation of model parameters. The same holds, although less markedly, for the metallic, Fermi-liquid-like state at small interaction strengths and small (or very large) t'/t . Despite the fact that the shape of $n(\mathbf{k})$ is distinct for the two liquid states, see Figs. 14(a) and (b), the differences are subtle. In order to distinguish between the FCI and metallic states, one would thus rather use the topological invariant of their ground states, see Sec. III C, or the criterion that the quasi-degenerate ground states remain separated from higher states for all fluxes, as used for Fig. 13, see above.

However, the charge-structure factor is very valuable in distinguishing the weakly correlated Fermi liquid from a CDW driven by Coulomb repulsion. At $\nu = 2/3$ and $t'/t = 0.1 < 0.18$, away from the FCI regime, two peaks appear in $n(\mathbf{k})$ and increase continuously upon increasing V/t , see Fig. 14(d). When choosing $t'/t = 0.2$ near the maximal flatness [see Fig. 14(c)] or $t'/t = 0.35$ with bad FS nesting [see Fig. 14(f)], the peaks only begin to grow for large V , where ground-state behavior upon flux insertion changes: a full gap is only obtained for lattice sizes commensurate with the ordering pattern, like the 3×6 and 6×6 lattices, but not on more general lattices. This indicates that the FCI state breaks down and is replaced by a CDW. The peaks observed in $n(\mathbf{k})$ for $\nu =$

$2/3$ grow with V , supporting their relation to a CDW. Their wave vectors correspond to a state where particles sit at NNN sites on the triangular lattice, i.e., to the regular charge pattern compatible with a filling of $\bar{n} = \nu/2 = 1/3$ of the triangular lattice. As can be seen in Fig. 12(d), this pattern avoids any penalty due to NN Coulomb interaction V and large enough $V \gg t, t'$ will thus eventually induce such a charge distribution.

The phase diagrams in Fig. 13 clearly show that the band flatness parametrized by M is itself not a reliable indicator for the stability of FCI states, as has also been pointed out recently in a different case.³⁰ The energy gap for $\nu = 1/3$ is rather symmetric with respect to the highest figure of merit, but the phase boundary determined by requiring a full gap over all momentum sectors and for all fluxes shows that the FCI states are somewhat more stable for larger t'/t . In the case of $\nu = 2/3$, the asymmetry is far more striking; as one can see in Fig. 13(b), FCI states require rather flat bands with $M \approx 13$ for $t'/t < 0.2$, but extend to a band with a width comparable to the gap separating it from its counterpart for $t'/t > 0.2$. Having rather flat bands indeed makes it easier for small V/t to induce FCI states both at $\nu = 1/3$ and $\nu = 2/3$, even though the optimal M is still not quite the largest, at least for our system sizes. As soon as the bands acquire some dispersion, however, features beyond band flatness, in our case FS nesting, can strongly influence the stability of FCI states by favoring competing states, in our case a CDW. Another key feature, which extends previous results,³⁰ is that in the case of competition between FCI and other phases, perfect band flatness is not necessarily the ideal condition for the stability of FCI ground states.

Before passing, a few more comments on the phase diagram have to be made. Ideally, a ground-state property would be used to determine the phase boundaries. One such property, which is sensitive to phase transitions, is the ground-state fidelity, defined as a measure of the overlap $\langle \psi(\alpha) | \psi(\alpha + \delta\alpha) \rangle$, where ψ is the ground-state wave function and α is a control parameter varied in small steps $\delta\alpha$. Phase transitions are then marked by a divergence in the fidelity at the transition point. Having calculated the ground-state fidelity upon varying interaction strength and band flatness for the cases presented here, we find that such divergences occur only at points where ground-state level crossings also occur, so the fidelity does not provide any extra information compared to the eigenvalue spectra. Furthermore, it has recently been shown that the fidelity on finite systems can fail to register topological phase transitions, e.g., between a FQH-like state and a Fermi liquid.⁶⁰

IV. SUMMARY AND CONCLUSIONS

Based on an earlier investigation,²² we have illustrated extensively how FCI states can emerge in a strongly correlated multiorbital model and have shown how an ef-

fective spinless one-orbital model with nearly flat bands and non-zero Chern number $C = \pm 1$ arises as the low-energy limit of Kondo-lattice and Hubbard models for t_{2g} orbitals on a triangular lattice. NN Coulomb interaction V then stabilizes states with all the characteristics of FCI states: the lowest eigenvalues have a near degeneracy corresponding to the denominator of the filling fraction and show spectral flow without closing of the energy gap. We have, moreover, demonstrated that the states of the ground-state manifold of this phase have a non-zero Hall conductivity, which is shown to be precisely quantized and equal to the filling fraction, in units of e^2/h . The exact quantization of the Hall conductivity holds also when FCI states are not ground states, and survives when the many-body Berry curvature is not a particularly flat function.

Deviating from the exact filling fraction $\nu = 1/3$ by either removing electrons or increasing the system size, we found indications of fractional quasihole statistics in the eigenvalue spectra, by application of the state-counting rule elaborated in Ref. 31. The eigenvalue spectra contain features that remind one of both the hierarchy and the composite fermion pictures of FQH states, therefore pushing the correspondence between FCI and FQH states one step further.

Since in the present context the magnetic texture is generated by strongly correlated itinerant electrons, imperfections in this texture are to be expected. We therefore investigate the impact of a localized impurity that mixes states across momentum sectors. Disorder causes splitting of the energy levels corresponding to the degenerate FCI ground states, thus making these states inequivalent in finite systems. However, the gap between these states and the excited-state spectrum remains open and their average Hall conductivity remains accurately fixed to the value of the filling fraction, even though the Hall conductivities of the individual states deviate from that value. This behavior illustrates the topological protection of the FCI states.

Finally, we address the robustness of FCI states with respect to band flatness, interaction strength, filling and FS nesting. Very flat bands indeed turn out to require the weakest interaction to produce an FCI state, corroborating the figure of merit M [see Eq. (10)] as a good first step in assessing candidate systems. As soon as one deviates from this limit, however, additional properties of the system become crucial: in contrast to a perfectly flat LL, strong particle-hole asymmetry can arise on a lattice, because some fillings allow CDWs more easily than others. In addition, a CDW is favored by FS nesting and this in turn reduces the stability range of the FCI states. Nevertheless, it turns out that FCI states can be obtained if either of the following conditions is met: (i) very flat bands, even near nesting and at a filling favorable to a CDW, and (ii) even rather dispersive bands, if the filling fraction or the absence of FS nesting are unfavorable to a CDW. This flexibility makes FCI states appear more realistic.

ACKNOWLEDGMENTS

This work was supported by the Deutsche Forschungsgemeinschaft under the Emmy-Noether program (S.K.

and M.D.) and the Interphase Program of the Dutch Science Foundation NWO/FOM (JV). We thank J. van den Brink for helpful discussions and B. A. Bernevig for insightful comments.

-
- ¹ R. B. Laughlin, *Phys. Rev. B* **27**, 3383 (1983).
² F. D. M. Haldane, *Phys. Rev. Lett.* **51**, 605 (1983).
³ B. I. Halperin, *Phys. Rev. Lett.* **52**, 1583 (1984).
⁴ D. C. Tsui, H. L. Stormer, and A. C. Gossard, *Phys. Rev. Lett.* **48**, 1559 (1982).
⁵ F. Wilczek, *Phys. Rev. Lett.* **49**, 957 (1982).
⁶ F. D. M. Haldane, *Phys. Rev. Lett.* **67**, 937 (1991).
⁷ C. Nayak, A. Stern, M. Freedman, and S. Das Sarma, *Rev. Mod. Phys.* **80**, 1083 (2008).
⁸ D. R. Hofstadter, *Phys. Rev. B* **14**, 2239 (1976).
⁹ G. S. Kliros and N. D'Ambrumenil, *J. Phys. C: Solid State Phys.* **3**, 4241 (1991).
¹⁰ F. D. M. Haldane, *Phys. Rev. Lett.* **61**, 2015 (1988).
¹¹ X.-L. Qi, Y.-S. Wu, and S.-C. Zhang, *Phys. Rev. B* **74**, 085308 (2006).
¹² C.-X. Liu, X.-L. Qi, X. Dai, Z. Fang, and S.-C. Zhang, *Phys. Rev. Lett.* **101**, 146802 (2008).
¹³ K. Ohgushi, S. Murakami, and N. Nagaosa, *Phys. Rev. B* **62**, 6065 (2000).
¹⁴ I. Martin and C. D. Batista, *Phys. Rev. Lett.* **101**, 156402 (2008).
¹⁵ E. Tang, J.-W. Mei, and X.-G. Wen, *Phys. Rev. Lett.* **106**, 236802 (2011).
¹⁶ K. Sun, Z. Gu, H. Katsura, and S. Das Sarma, *Phys. Rev. Lett.* **106**, 236803 (2011).
¹⁷ T. Neupert, L. Santos, C. Chamon, and C. Mudry, *Phys. Rev. Lett.* **106**, 236804 (2011).
¹⁸ D. N. Sheng, Z.-C. Gu, K. Sun, and L. Sheng, *Nat. Comm.* **2**, 389 (2011).
¹⁹ Y.-F. Wang, Z.-C. Gu, C.-D. Gong, and D. N. Sheng, *Phys. Rev. Lett.* **107**, 146803 (2011).
²⁰ N. Regnault and B. A. Bernevig, *Phys. Rev. X* **1**, 021014 (2011).
²¹ Y. L. Wu, B. A. Bernevig, and N. Regnault, *Phys. Rev. B* **85**, 075116 (2012).
²² J. W. F. Venderbos, S. Kourtis, J. van den Brink, and M. Daghofer, *Phys. Rev. Lett.* **108**, 126405 (2012).
²³ T. Liu, C. Repellin, B. A. Bernevig, and N. Regnault, *arXiv:1206.2626v1* (2012).
²⁴ A. M. Läuchli, Z. Liu, E. J. Bergholtz, and R. Moessner, *arXiv:1207.6094v1* (2012).
²⁵ M. Trescher and E. J. Bergholtz, *arXiv:1205.2245v3* (2012).
²⁶ S. Yang, Z.-C. Gu, K. Sun, and S. D. Sarma, *arXiv:1205.5792v2* (2012).
²⁷ Y.-F. Wang, H. Yao, C.-D. Gong, and D. N. Sheng, *Phys. Rev. B* **86**, 201101(R) (2012) *arXiv:1204.1697v1* (2012).
²⁸ Z. Liu, E. J. Bergholtz, H. Fan, and A. Läuchli, *Phys. Rev. Lett.* **109**, 186805 (2012).
²⁹ A. Sterdyniak, C. Repellin, B. A. Bernevig, and N. Regnault, *arXiv:1207.6385v1* (2012).
³⁰ A. G. Grushin, T. Neupert, C. Chamon, and C. Mudry, *Phys. Rev. B* **86**, 205125 (2012).
³¹ B. A. Bernevig and N. Regnault, *Phys. Rev. B* **85**, 075128 (2012).
³² X.-L. Qi, *Phys. Rev. Lett.* **107**, 126803 (2011).
³³ Y.-L. Wu, N. Regnault, and B. A. Bernevig, *Phys. Rev. B* **86**, 085129 (2012).
³⁴ C. H. Lee, R. Thomale, and X.-L. Qi, *arXiv:1207.5587v2* (2012).
³⁵ G. Murthy and R. Shankar, *arXiv:1207.2133v2* (2012).
³⁶ G. Murthy and R. Shankar, *arXiv:1108.5501v2* (2012).
³⁷ S. A. Parameswaran, R. Roy, and S. L. Sondhi, *Phys. Rev. B* **85**, 241308 (2012).
³⁸ M. O. Goerbig, *Eur. Phys. J. B* **85**, 15 (2012).
³⁹ D. Xiao, W. Zhu, Y. Ran, N. Nagaosa, and S. Okamoto, *Nat. Comm.* **2**, 596 (2011).
⁴⁰ P. Ghaemi, J. Cayssol, D. N. Sheng, and A. Vishwanath, *Phys. Rev. Lett.* **108**, 266801 (2012).
⁴¹ J. W. F. Venderbos, M. Daghofer, and J. van den Brink, *Phys. Rev. Lett.* **107**, 116401 (2011).
⁴² Y. Akagi and Y. Motome, *J. Phys. Soc. Jpn.* **79**, 083711 (2010).
⁴³ S. Kumar and J. van den Brink, *Phys. Rev. Lett.* **105**, 216405 (2010).
⁴⁴ Y. Kato, I. Martin, and C. D. Batista, *Phys. Rev. Lett.* **105**, 266405 (2010).
⁴⁵ H. F. Pen, J. van den Brink, D. I. Khomskii, and G. A. Sawatzky, *Phys. Rev. Lett.* **78**, 1323 (1997).
⁴⁶ W. Koshibae and S. Maekawa, *Phys. Rev. Lett.* **91**, 257003 (2003).
⁴⁷ W. A. Harrison, *Electronic Structure and the Properties of Solids* (W. H. Freeman, San Francisco, 1980).
⁴⁸ J. C. Slater and G. F. Koster, *Phys. Rev.* **94**, 1498 (1954).
⁴⁹ E. Dagotto, *Nanoscale Phase Separation and Colossal Magnetoresistance* (Berlin: Springer, 2002).
⁵⁰ C. Lanczos, *Journal Of Research Of The National Bureau Of Standards* **45**, 255 (1950).
⁵¹ C. Lanczos, *Journal Of Research Of The National Bureau Of Standards* **49**, 33 (1952).
⁵² X. G. Wen and Q. Niu, *Phys. Rev. B* **41**, 9377 (1990).
⁵³ R. Tao and Y. S. Wu, *Phys. Rev. B* **30**, 1097 (1984).
⁵⁴ S. He, X. C. Xie, and F.-C. Zhang, *Phys. Rev. Lett.* **68**, 3460 (1992).
⁵⁵ M. D. Johnson and G. S. Canright, *Phys. Rev. B* **49**, 2947 (1994).
⁵⁶ J. K. Jain, *Phys. Rev. Lett.* **63**, 199 (1989).
⁵⁷ Q. Niu, D. J. Thouless, and Y.-S. Wu, *Phys. Rev. B* **31**, 3372 (1985).
⁵⁸ D. Xiao, M. C. Chang, and Q. Niu, *Rev. Mod. Phys.* **82**, 1959 (2010).
⁵⁹ D. N. Sheng, X. Wan, E. H. Rezayi, K. Yang, R. N. Bhatt, and F. D. M. Haldane, *Phys. Rev. Lett.* **90**, 256802 (2003).
⁶⁰ S. Yang, K. Sun, and S. Das Sarma, *Phys. Rev. B* **85**, 205124 (2012).